CZECH TECHNICAL UNIVERSITY IN PRAGUE
Faculty of Civil Engineering

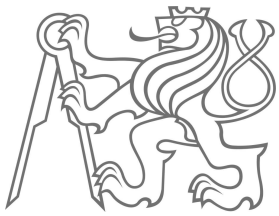

2009/2010

Master thesis

Micromechanical analysis of alkali activated fly ashes

Mikromechanická analýza alkalicky aktivovaných popílků

Author: **Petr Hlaváček**

Supervisor: **Doc. Ing. Vít Šmilauer, Ph.D.**
Department: **Department of Mechanics**

Prohlášení

Prohlašuji, že jsem tuto diplomovou práci vypracoval samostatně, pouze za odborného vedení školitele Doc. Ing. Víta Šmilauera, Ph.D.

Dále prohlašuji, že veškeré podklady ze kterých jsem čerpal jsou uvedeny v referencích.

V Praze dne 21.5.2010

Poděkování

Chtěl bych zejména poděkovat mému školiteli, Doc. Vítu Šmilauerovi nejen za jeho trpělivost a vstřícnost při podnětných konzultacích ale také za pomoc s vytvářením práce v prostředí LaTeX. Dále bych rád poděkoval Doc. J. Němečkovi, RNDr. L. Kopeckému a Doc. F. Škvárovi za poskytnutí výsledků výzkumu a Ing. R. Šulcovi za zařízení betonáže. V neposlední řadě patří dík mé rodině a blízkým, bez jejichž podpory a pochopení by práce nemohla vzniknout.

Výsledky této práce byly finančně podpořeny grantem Studentské grantové soutěže ČVUT č. SGS10/135/OHK1/2T/11 a Grantové agentury České republiky, grant č. 103/08/1639.

Contents

List of Figures

List of Tables

Annotation

One of the main objectives of this work is a formulation of model, which describes evolution of chemical phases occurring during alkali activation of fly ash. The phases are fly ash skeleton, fly ash voids, solid gel particles and open porosity. The volume evolution of open porosity during curing period was determined. Using the open porosity and fly ash evolution formulated a microstructure model. The micromechanical properties of the phases were determined by homogenization process using the experimentally measured Young's moduli at macro level (nondestructive testing of Alkali Activated Fly Ash AAFA prisms). The result of the work is the model of phases evolution during curing of AAFA and the micromechanical characteristics of the phases. In addition a diffusion coefficient for Na^+ ion transport in AAFA was determined.

Anotace

Práce se zabývá formulací modelu popisujícího vývoj chemických fází během alkalické aktivace popílku. Fázemi jsou skelet popílku, póry popílku, gelové pevné částice a otevřená porozita. Experimentálně byl stanoven vývoj objemového zastoupení otevřené porozity během zrání alkalicky aktivovaného popílku. Pomocí porozity a vývoje zastoupení popílku byl formulován mikrostrukturní model. Mikromechanické vlastnosti fází byly stanoveny nanoindentací a pomocí homogenizačních technik byly převedeny na Youngův modul celého materiálu. Tato hodnota byla porovnána s experimentálně změřenými elastickými moduly na makro úrovni, nedestruktivní zkoušky alkalicky aktivovaného popílku (AAFA) . Výsledkem práce je model vývoje fází během zrání AAFA. Zároveň jako další část práce byl stanoven difúzní koeficient pro transport Na^+ iontů.

1 Introduction and scope of the work

1.1 Fly ash as a by product of energy production

Rapid economical growth and technical development in 19th century caused improvement of standard of living. One of the greatest benefits was electrification. First commercial power station in the world was launched in New York by Thomas Alva Edison in 1882. This power station worked on the principle of dynamo which was driven by steam engine and it could power maximally 1000 Edison's light bulbs. The first power station in the Czech Republic was build by František Křižík in Prague on Žižkov in the year 1888. In the same year another power station in Písek was build by the same man F. Křižík and the electrification of the town followed. Písek was the first town in Czech lands where permanent street lighting was installed.

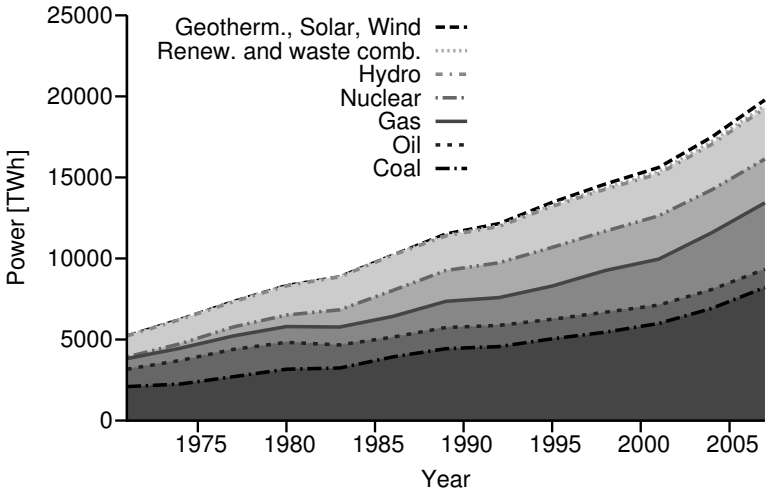

Figure 1: World electricity generation by fuel. Taken from OECD/IEA 2009

Energy demands growth trough the years and the spreading of electric energy required increase of it's production. Many power stations were built and coal has been used as one of the cheapest and most accessible energy source. The Fig. 1 shows development of production of electrical energy divided according to the energy source between 1970 and 2007. In 2007 comes more than one third of electrical energy in the world from coal combustion plants. Moreover in the last years rose up the installed power of coal combustion plants significantly. In these plants occurs real ecological problem with the solid burning residua (with the fly ash).

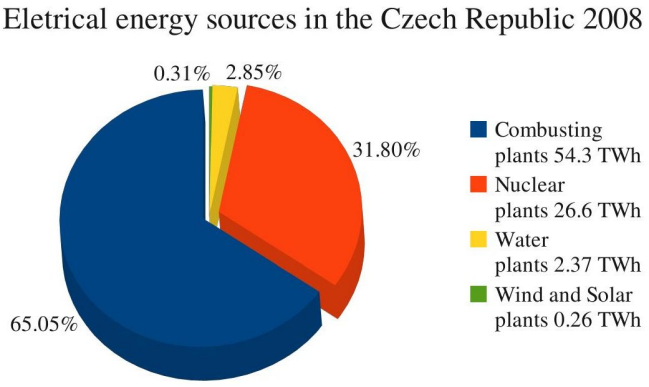

Figure 2: Czech electricity generation by fuel in 2008. Data from CSU

In the comparison with the world is the review of electrical energy production in the Czech Republic more unsuitable, see Fig. 2. The coal combustion plants product there 65% of all electrical energy (2008, source CZSO, the statistics 2009 has not been published yet).

The power of coal combustion plants in the Czech Republic is 54.3 TWh/year, data from [CZSO, 2010]. The lower heating values of different types of coal are mentioned in the Tab. 1.

Material	Heating value (HV)		Combustion	Solid burning
	[MJ/kg]	[kWh/kg]	efficiency (η)	residua
Brown coal	13	3.611	30-40%	10-30%
Black coal	22	6.111	max. 45%	10-15%

Table 1: Coal heating value, burning efficiency and amount of solid residua.

Let us consider the efficiency of combustion as 30% [CEZ, 2010]. Simple calculation gives the value of the burned coal mass in the Czech Republic in 2008,

$$\frac{\mathrm{P}}{\mathrm{HV}\cdot\eta} = \frac{54.3\ \mathrm{TWh/year}}{3.611\ \mathrm{kWh/kg}\cdot 0.3} = 50.13\cdot 10^{9}\ \mathrm{kg/year}.$$

This result of 50.13 millions tons of burned coal in 2008 in the Czech Republic is in good correspondence with the value given by the Czech Statistical Office. The official number is 46.95 millions tons of coal used in power plants, from which 42.6 of brown coal and 4.35 of black coal, [CZSO, 2010]. Assuming the

mass of solid burning residua (of the fly ash respectively) is 20% of the mass of the coal. The production of fly ash is in the Czech Republic annually

$$50.13 \cdot 10^9 \text{ kg} \cdot 0.2 \approx 10 \cdot 10^9 \text{ kg} = 10 \text{ million tons.}$$

The same calculation can be done for the estimation of worldwide fly ash production. In this calculation problem occurs with the ratio of black to brown coal usage in the world electrical energy production. Due to this fact it will be computed the lower and upper estimation of annual worldwide fly ash production. Several possible values for different ratii are given in the Tab. 2. In 2007 was transformed 8210 TWh energy worldwide in coal combustion plants, see Fig. 1.

Ratio	1:0	3:1	2:1	1:1	1:2	1:3	0:1
FA [mil. tons]	1516	1230	1135	944	754	659	373

Table 2: Estimation of worldwide fly ash production.

Let us consider the worldwide ratio is 1:1, then the progress of FA production during years is shown on the Fig. 3. Our calculation of FA worldwide production is in suitable correspondence with the value used in literature. Fernández-Jiménez is considering that in 2010 there will be production of 800 millions tons of fly ashes in the world, [Fernández-Jiménez and Palomo, 2005].

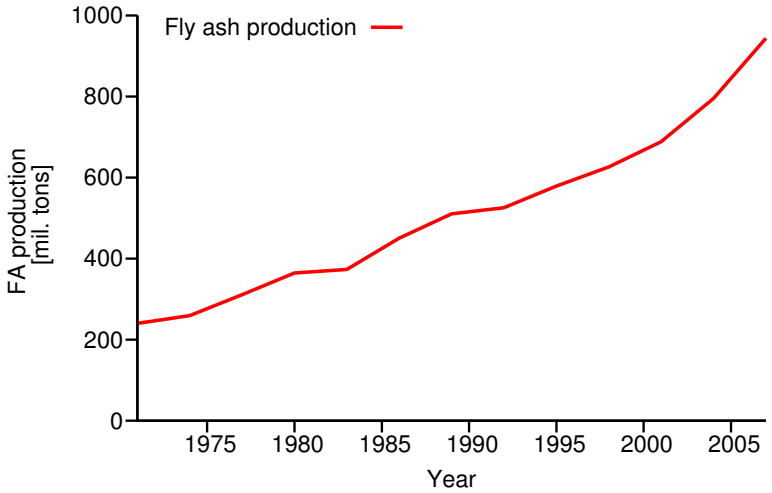

Figure 3: World fly ash production.

The shape of the fly ash particles is illustrated on the BSE image, see Fig. 4

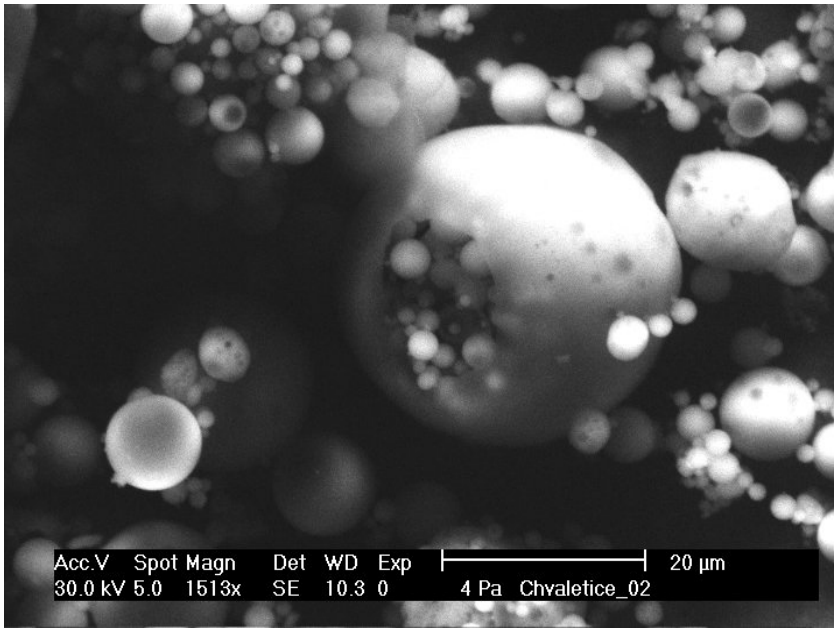

Figure 4: BSE image of raw fly ash. Image by L. Kopecký

1.2 Utilization of fly ash

Production of the fly ashes is nowadays one of the greatest ecological burdens. Only a small part of them is used at present (20-30%). The rest is stored in landfills where occurs real space problem and also there is not negligible risk of air and ground water pollution. Researchers are trying to find ways how to use these materials or liquidate them ecologically. The main aim is to improve and protect our environment. One of the possibilities is to use the fly ash as an alternative to ordinary concrete. It is possible to use the FA in the alkaline activation process. Alkaline activation means mixing the FA with sodium hydroxide (NaOH) and water glass. The reaction product is an amorphous alumino-silicate gel. Recent basic research shows that the Alkaline Activated Fly Ash (AAFA) has high potential to replace ordinary concrete in special applications due to acid resistance, fire resistance, low drying shrinkage, low calcium content, improved durability, no alkali-silica reaction, freeze/thaw performance or lower creep induced by mechanical load [Wallah and Rangan, 2006].

Production of ordinary Portland cement is linked with high energy demands and with high ecological treatment. By the production of 1 ton of Portland cement there is a by product of almost 1 ton of CO_2. A sintering process in the cement production runs at 1450°C and the energy required for production of 1 ton of material is almost 1000 kWh. Following table Tab. 3 shows the energy demands comparison between one ton of alkali activated fly ash (AAFA) and one ton of cement, data from [Kynčlová, 2006]. In case of AAFA means the value the energy needed for the production of activator used in the alkali activation.

Cement	3.5 GJ	972 kWh
AAFA	1.33 GJ	370 kWh

Table 3: Fly ash and cement energy demands for one ton of material, data from [Kynčlová, 2006].

Fig. 5 shows the evolution of cement production worldwide. Production data report the sum of Portland, natural, masonry, and slag or pozzolanic cement (all hydraulic cements). In 2008 the production was 2850 million tons [Survey, 2009]. In the case that all produced fly ash can be utilized as building material, 1/3 of concrete can be saved. Hopefully in near future the alkali activated fly ash should replace partially the really non-ecological ordinary concrete.

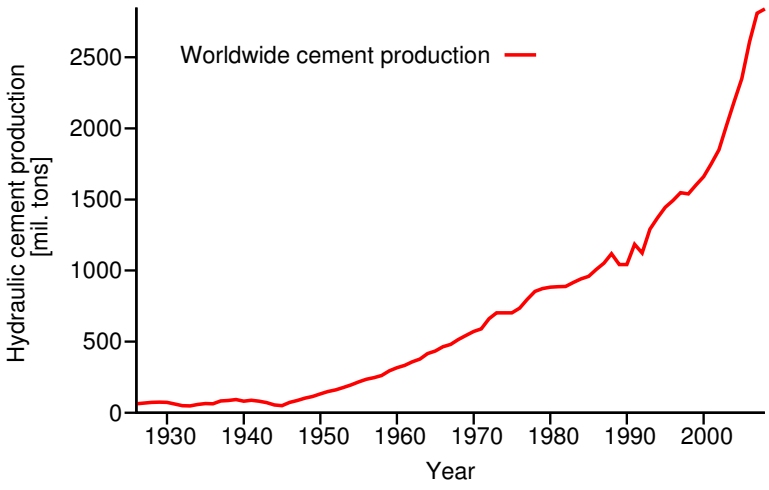

Figure 5: World cement production.

1.3 History of alkali activation

The history of alkali activation goes to the ancient Roman and Egyptian time [Glukhovsky, 1959]. Glukhovsky concluded, that in the ancient time they used aluminosilicate calcium hydrates binder materials not so different from today concretes. Concurrently Davidovits introduced a controversial theory that the pyramids in Egypt are not made from a natural rock but from a activated limestone sand. He suggested it's a mixture of calcium hydroxide, limestone sand, sodium carbonate and water. He proofs this theory by the fact that calcium fossilized layers in the blocks in pyramids are oriented not regularly as in the case of natural sediments but are oriented absolute randomly. The summary about the Davidovit's Egyptian investigation is introduced for example in [Škvára et al., 2008], but unfortunately without definitive conclusion.

Davidovits in 1979 was the first author, who introduced the term "geopolymer" for alkali activated product derived from aluminosilicate-bearing raw material metakaolin. He was first in modern history, who used the calcium-free systems based on calcined clays. He introduced the word "geopolymer" as a name for the new materials originated from metakaolin alkali activation. The term "POLYMER" is used because these materials are polymers. Polymers means they transform, polymerize and harden at low temperature. And "GEOpolymers" because these materials are high and stable at high temperature, non-inflammable and inorganic. In this work the term "N-A-S-H gel" will be used further for reaction products instead of the name "geopolymer". The term gel is more general, includes also the geopolymers and is well-established in literature [Němeček et al., 2009].

Davidovits was not the first author who made the research into alkaline activated materials. In 1950's professor Gluchovskij conducted detailed research into this materials in Ukraine. He developed a "soil-cement" which was obtained from ground aluminosilicate mixed with industrial wastes rich on alkalies. He called this materials as "gruntosilikaty" and " gruntocementy" [Gluchovskij, 1959]. His most important investigations were first the identification of hydration products made from calcium silicate hydrates and calcium and sodium aluminosilicate hydrates and second the identification that alkali activated clay minerals are forming aluminum silicate hydrates. In 1958 he provides a first described application of the new material, the experimental house built from alkali activated blocks.

In the following Tab. 4 the most important investigations in branch of alkali activated materials are introduced. The list is taken from [Pecheco-Torgal et al., 2008].

Author	Year	Significance
Feret	1939	Slags used for cement
Purdon	1940	Alkali-slag combinations
Glukhovsky	1959	Theoretical basis ans development of alkaline cements
Glukhovsky	1965	Fist called "alkaline cements"
Davidovits	1979	"Geopolymer" term
Malinowski	1979	Ancient aquaducts characterized
Forss	1983	F-cement (slag-alkali-superplasticizer)
Langton and Roy	1984	Ancient building materials characterized
Davidovits and Sawyer	1985	Patent of "Pyrament" cement
Krivenko	1986	DSc thesis, R_2O–RO–SiO_2–H_2O
Malolepsy and Petri	1986	Activation of synthetic melilite slags
Malek. et al.	1986	Slag cement-low level radioactive wastes forms
Davidovits	1987	Ancient and modern concretes compared
Deja and Malolepsy	1989	Resistance to chlorides shown
Kaushal et al.	1989	Adiabatic cured nuclear wastes forms from alkaline mixtures
Roy and Langton	1989	Ancient concretes analogs
Majundar et al.	1989	$C_{12}A_7$ – slag activation
Talling and Brandstetr	1989	Alkali-activated slag
Wu et al.	1990	Activation of slag cement
Roy et al.	1991	Rapid setting alkali-activated cements
Roy and Silsbee	1992	Alkali-activated cements: an overview
Palomo and Glasser	1992	CBC with metakaolin
Roy and Malek	1993	Slag cement
Glukhovsky	1994	Ancient, modern and future concretes
Krivenko	1994	Alkaline cements
Wang and Scrivener	1995	Slag and alkali-activated microstructure

Table 4: Important investigation results about alkali activated binders.

1.4 Process of alkali activation

Investigation in this field had accelerated first with Davidovits who developed and patented binders obtained from the alkali activation of metakaolin.

Davidovits also introduced a model of the geopolymer gel which consists of three-dimensional structure, built from SiO_4 and AlO_4 tetrahedral connected by shared O atoms and forming polymeric chains [Davidovits, 1999]:

$$M_n[-(SiO_2)_z - AlO_2]_n \cdot wH_2O,$$

where is the symbol M for sodium, potassium or calcium supplied with alkali activator and fly ash, n is the degree of polymerization, z indicates the amount of SiO_2 monomer units in the gel (typically between 1 and 3) and w is the amount of binding water. Further forms [Fernández-Jiménez et al., 2006b] the basic of the main objectives of alkaline activation process and introduced a descriptive model of this research extended to certain quantities. [Zhang et al., 2009] proposed more advanced structural model.

Fernández-Jiménez, [Fernández-Jiménez et al., 2006b], proposed an advanced AAFA model, which distinguishes three stages of reaction:

1. dissolution stage,
2. induction period,
3. silicon incorporation stage.

The mechanism of geopolymer formation was also described by Davidovits [Davidovits, 1999], Deventer [Xu and van Deventer, 2000] and Fernández-Jiménez [Fernández-Jiménez et al., 2004, Fernández-Jiménez et al., 2006b]. The following list is taken from [Němeček, 2009], formation of N-A-S-H gel:

1. the highly alkaline liquid environment causes the dissolution of Si and Al minerals from the fly ash, especially its vitreous components,
2. after the dissolution, the Al and Si precursor ions are transported within the highly alkaline water environment, reacting with a part of water and alkalies, forming the monomer units,
3. the monomers enter polycondensation/polymerization stage, releasing certain amount of water back to the system.

The first stage - dissolution - is the chemical attack on fly ash particle. The fly ash is a porous material which is produced in combustion power plants. The process leaves the spherical shapes of fly ash with entrapped gases and partially unburnt carbon, see Fig. 4. Although the fly ash particles appears as solid spheres in electron microscope, [Sakamoto et al., 2003] shows that they are very often in the form of a hollow thin shell. Thus the

dissolution opens partially the inner porosity and the alkaline solution may enter the interior of the fly ash particle [Fernández-Jiménez et al., 2004]. The rate depends primarily on the pH of activator and the amount of vitreous phase content in fly ash [Fernandez-Jimenez and Palomo, 2003].

In the second stage there is a result of formation of monomer units that start to form nuclei for further grow. Fernández-Jiménez shows, that metastable gel is formed around fly ash particles, from reactive aluminum originated from fly ash, [Fernández-Jiménez et al., 2006b].

The third stage of polymerization occurs when the nuclei reach critical size. It is the growth or silicon incorporation stage. When the gel from solution consumes a precursor is this stage really slow, because the new supply is a diffusion-controlled process. The gel creates a barrier around fly ash particle and prevents the alkaline solution to enter the first and second stage. At this time the worse soluble Si is incorporated in the gel, what causes the substantial strength gain [Fernández-Jiménez et al., 2006a]. [Hardjito and Rangan, 2005] shows that the mixing water is consumed during the formation of precursor and is given back at the polycondensation/polymerisation stage, expelled from the nanometer level.

1.5 The aim of the work

The objectives and methods of this work are focused on alkali activation of fly ash (AAFA). The main steps are:

1. Quantification of open porosity development during the curing process of the AAFA. The porosity development are based on measured differences in sample densities.

2. Formulation of volumetric model of phases during the process of alkali activation. Four dominant phases are considered in the model.

3. Identification and alignment of intrinsic elastic properties to the four volumetric phases.

4. Formulation of multi-scale micromechanical model suitable for elastic properties. These will be upscaled with known homogenization techniques to the macro level and the results will be compared with experimentally measured values.

5. Determination of diffusion coefficient for Na^+ leaching from the the AAFA material. Efflorescence presents a major problem of AAFA materials today, the determination of the diffusion coefficient helps to design structure elements with leaching mitigation.

6. Casting of large scale structural element. This experiment should verify and monitor workability, durability, freeze/thaw performance and esthetical appearance of AAFA concrete.

2 Materials and methods

2.1 Fly ash

The fly ash is a by product from energy production in coal combustion plants. See the introduction for deeper analysis of fly ash production. The origin of FA by high temperature causes the particles look like small balls, see Fig. 4 and have usually thin hollow shell, [Sakamoto et al., 2003]. The pore distribution curve obtained from MIP (Mercury intrusion porosimetry), Fig. 6, compares several types of fly ashes and shows a significant peak at about one μm what is in good correspondence with the hypothesis of the particle shape.

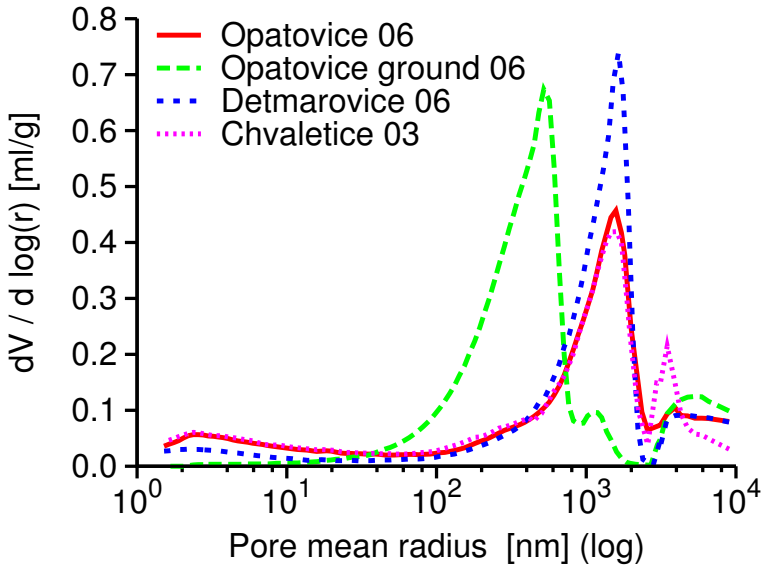

Figure 6: Pore distribution curve in the non-activated fly-ash and metakaolin

A low calcium fly ash class F originated from the brown coal power plant Chvaletice, the Czech Republic, was utilized for experiment. The Blaine specific surface of this raw fly ash is 210 m^2/kg. Chemical composition of the FA is introduced in Tab. 5.

For some experiments the fly ash was ground in a small-scale ball mill, in the others experiments was utilized raw fly ash. Fig. 7 shows the evolution of particle diameter distribution with respect to the time of grinding. The grinding causes crushing of the hollow cenospheres and thus reduction of

the initial porosity. The grinding time of the ground fly ash utilized in experiments was 45 minutes.

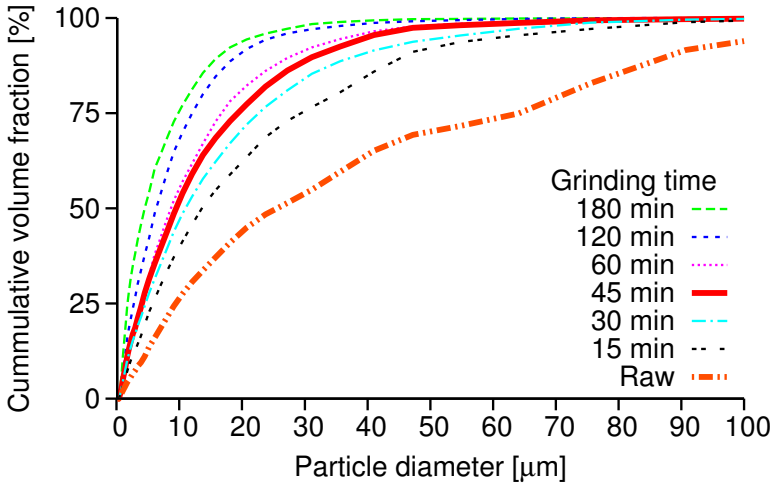

Figure 7: Particle size distribution of fly ash, dependence on grinding time

2.2 Metakaolin

The metakaolin is a thermally activated clay containing substantial volume of clay minerals as kaolinite. The thermal treatment is an endothermic process which runs at temperature between 600°C and 900°C. By this temperature kaolinite looses water through dehydroxilization. A large amount of energy (150 kJ/mol) [Földvári, 1997] is consumed to disengage the chemically bonded hydroxyl anions. Thus the metakaolin has an high energetic state and is highly reactive. Chemical composition of the metakaolin is introduced in the Tab. 5.

The metakaolin used in the experiment originates from České Lupkové závody a.s., Nové Strašecí the Czech Republic. The particle size distribution is depicted in Fig. 8. The Blaine surface area is about 350 m^2/kg.

	SiO_2	Al_2O_3	Fe_2O_3	CaO	TiO_2	K_2O
Ground fly ash	51.9	32.8	6.3	2.7	1.89	2.12
Metakaolin	48.66	47.41	1.33	0.03	1.99	0.15

Table 5: The chemical composition of ground fly ash and metakaolin (wt.%)

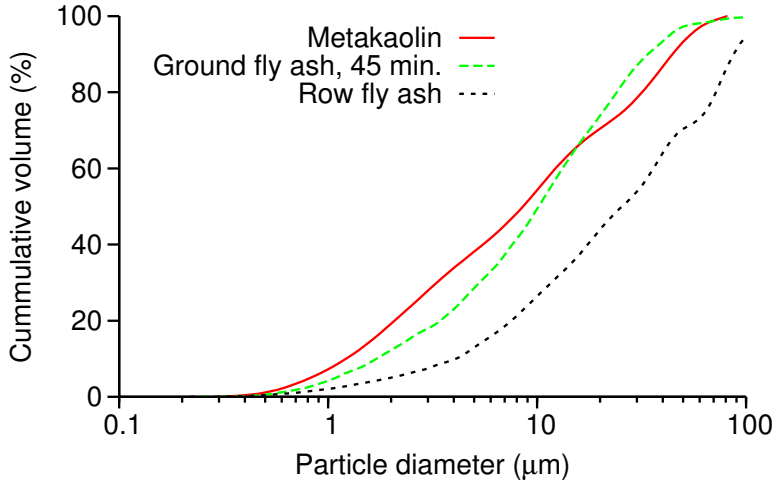

Figure 8: Particle size distribution of ground fly ash and metakaolin

2.3 Activating solution

A strongly alkaline liquid is usually utilized as an activator in the alkali activation . The main phase needed for activation is a hydroxyl group (OH^-). NaOH and KOH are commonly used. NaOH is cheaper than the KOH and provides improved mechanical properties. Theoretically can be used also LiOH, but high cost limits the applicability. Overdosing the activator improves workability of mixture, but causes leaching problems and efflorescence on the final material.

The alkali activation can theoretically take place without any other substance in the activator, but mechanical properties of such system are really poor. Sufficient mechanical properties of the reaction product can be achieved by adding water glass to the activator. Thus in the following experiments the activator consists of sodium hydroxide and sodium water glass. Tab. 6 summarizes the in experiments used mixture of activator.

	Activator ratii		Activator to
	Na_2O/SiO_2 (-)	H_2O/Na_2O (-)	solid ratio (wt. %)
Raw fly ash	0.875	3.088	0.461
Ground fly ash	0.881	3.925	0.531
Metakaolin	1.669	2.743	1.416

Table 6: Mixture composition. Mass oxide ratii for activators and activator-to-solid mass ratii.

2.4 Sample manufacturing and curing

The manufacture of geopolymer samples took place in the laboratory of Department of Glass and Ceramics at the Institute of Chemical Technology in Prague. Three different precursors had been used for the sample preparation,

1. raw fly ash,
2. ground fly ash,
3. metakaolin.

The composition of the alkali-activator and the solution/ash ratio was previously optimized to yield a high compressive strength and good workability [Škvára et al., 2009]. The activator was prepared by NaOH pellets dissolving in the sodium water glass. In the Tab. 6 are summarized the mixtures compositions. The three independent parameters introduced here control the final properties of the mixture. Metakaolin requires significantly more activator to achieve a sufficient workability due to its higher surface area.

The precursor (fly ash or metakaolin) was intermixed with the activator. Mixing time took five minutes, after that the mixture was cast into 10 ml plastic ampoules 26 mm in diameter and 45 mm in height and gently vibrated for five minutes. After vibration were the ampoules hermetically closed by cover to avoid the water evaporation and cured.

Ambient-cured fly ash stayed at laboratory temperature $\approx 22°C$. The curing period took the time from one week up to six moths according to the type of following experiment.

Heat-cured fly ash and metakaolin specimens were exposed to 80°C for 12 hours prior to testing.

In summary, five sets of alkali activated specimens were produced.

1. Heat cured ground FA,
2. heat cured non-ground FA,
3. ambient cured ground FA,
4. ambient cured non-ground FA,
5. heat cured metakaolin.

2.5 Porosity assessment

Porosity determination is relatively difficult problem. As already mentioned, the fly ash particles are spheres [Sakamoto et al., 2003] often as a hollow thin shell. The first stage of alkaline reaction is the dissolution of this thin shell and that causes decrease of open porosity. First let us describe three different methods applied for porosity assessment:

1. **Mercury intrusion porosimetry** (MIP). For the MIP method, the specimen is crushed (the size of particles is in the range of millimeters) and suffused by mercury. By a zero pressure within the mercury bath a bulk density of the specimen is obtained. Subsequently the pressure rises and the intrusion volume is measured. The maximum pressure of the mercury bath is about 60000 psia (414 MPa). The MIP gives the pore distribution. The operating range of MIP is between 120 μm from the top and 3.2 nm from bottom.

2. **He pycnometry**. Crushed specimens are measured also in He pycnometry. The principle of He pycnometry is based on volume determination using the ideal gas law. Gas intrusion can be detected by the pressure change. The He pycnometry gives skeletal density. The resolution goes to the helium atom size (d $\approx$ 0.062 nm).

3. **Drying up and saturation by isooctane**, introduced by Perera [Perera et al., 2007]. The main advantage of this method are minimal requirements on a special laboratory equipment. Specimens in ampoules (d $\approx$ 22 mm) are cutted into approx. 4.5 mm thick slices, the dimensions of the slices are precise measured by a digital caliper and the volume is computed. Then the specimens are dried up in vacuum or by 105°C for seven days (until the mass stabilizes), precisely weighted and submerged into n-octane (non-polar liquid). The saturation takes three to five days. After that the slices are again weighted. Open porosity is calculated from the mass difference between the dry and saturated state and the known volume.

The MIP (Autopore III Micromeritics) and He pycnometry (Micromeritics AccuPyc 1330) measurements were carried out at Institute of Chemical Process Fundamentals of the Academy of Sciences of the Czech Republic. The method using drying and saturation took place in the local laboratory.

The isooctane measuring method provides different estimation of porosity then the MIP. The MIP, as mentioned above, does not care about the surface pores; the volume of specimen is measured by submersion into the Hg. On the other hand, the method using isooctane can not sufficiently describe the

small pores simply due to the size of the isooctane molecule Fig. 9. The other disadvantage of this method is that it works under ambient pressure. Some of the pores occurring after the activation in the gel can have shape like a bottle with a narrow neck. The pore itself can be relatively large, but the bottle does not allow the isooctane to penetrate inside, as to opposite MIP due to the high pressure which could break the thin shell of those pores.

It is necessary to mention that the true porosity is expected to be higher than the values obtained from those methods because of incomplete permeation of the agent into the pores.

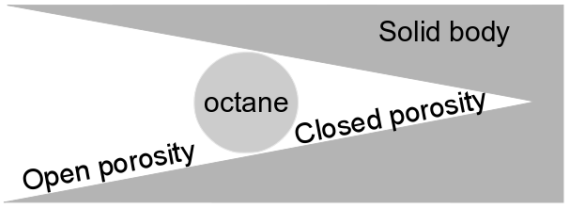

Figure 9: Porosity distribution compared with iso-octane molecule size. Molecule size defines a threshold between open (accessible) and closed (non-accessible) porosity.

Due to this limitations was implemented another approach combining the drying up known from the isooctane method and the He pycnometry. In this approach the porosity is calculated from known bulk density (the mass and the volume of sample with a well defined geometry in dry state) ρ^b_{FA} and skeletal density obtained from He pycnometry ρ^{sk}_{FA},

$$\Phi = 1 - \rho^b_{FA}/\rho^{sk}_{FA}. \tag{1}$$

2.6 Nanoindentation

The description of nanoindentation method is taken from [Šmilauer et al., 2010] and was performed in house by Jiří Němeček [Němeček et al., 2009]. Activated samples were cut to parallel slices of approx. 10 mm in thickness, polished on fine emery papers and polishing cloth, and cleaned in an ultrasonic bath. Nanoindentation was carried out in a series of grids of 10 x 10 = 100 imprints in three representative areas. The distance between individual indents varied between 10 and 50 μm. Nanoindentation measurements were performed in a load control regime using the CSM Nanohardness tester equipped with a Berkovich tip. The trapezoidal loading diagram was prescribed for all tests with a linear loading of 4 mN/min and lasting for 30 s, which produced the maximum load of

2 mN for all indents. Peak load of 2 mN led to maximum penetration depths ranging from 100 nm to 400 nm. Fig. 10 shows a typical force/penetration diagram for three identified material phases.

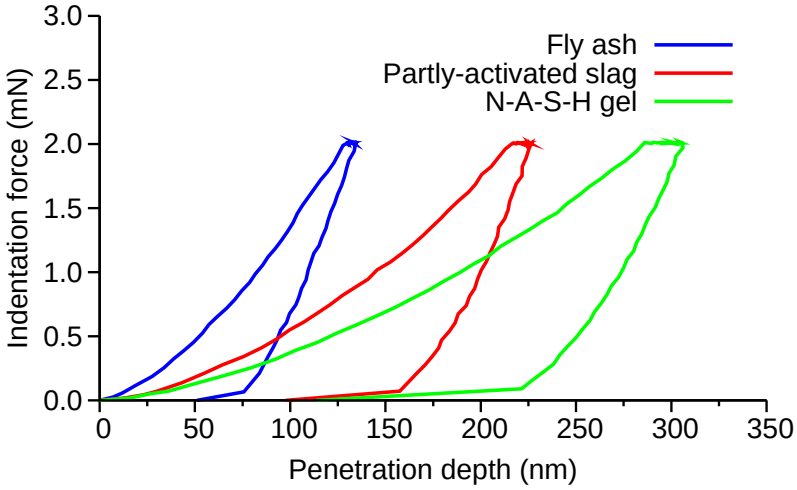

Figure 10: A typical nanoindentation diagram for alkali-activated fly ash.

The effective depth captured by the tip of the nanoindenter can be roughly estimated as three to four times of the penetration depth for the Berkovich indenter [Constantinides et al., 2006]. It yields the effective depth of around 1 μm from which the elasticity is obtained.

3 Multiscale micromechanical model for elastic properties of AAFA

The multiscale model is based on a volumetric model, nanoindentation experiment and homogenization techniques. The volumetric model for alkali-activation presents a stepping stone for the micromechanical analysis. Much inspiration comes from Portland cement. The nanoindentation sensing technique gives micromechanical elastic properties. The multiscale homogenization of the phases identified by volumetric model and nanoindentation result in the macro-level mechanical properties.

This section deals with interconnecting chemical and mechanical disciplines. First, porosity evolution in AAFA was measured. The intrinsic elastic properties were identified, the elasticity of the fractions is assumed to be independent on time. Second, a new volumetric model of alkali activation was formulated. Third, two-scale elastic homogenization combined with percolation upscales the intrinsic properties to the macroscopic scale.

The micromechanical model formulation consists from following steps.

1. Assessment of porosity development in the AAFA during activation and curing. This data had been measured experimentally and are introduced in next section.

2. Formulation of volumetric model based on the porosity development.

3. Alignment of micromechanical elastic intrinsic properties obtained from nanoindentation with the volumetric phases defined in the model.

4. Upscaling of the micromechanical data to the macro level using known homogenization techniques and comparing with the experimentally measured results.

3.1 Porosity of a three-phase medium

As mentioned above a problem with the pore size occurs when the porosity is measured by the isooctane. Some of the pores can be smaller than the molecule of the isooctane. This pores are called closed or non-accessible. The other pores are assuming to be for the isooctane accessible. The three-phase medium reflects the volume of non-accessible pores and allow better estimation of total porosity using the isooctane measuring method. It consists of following fractions,

1. closed porosity, non-accessible pores, described by volume V_1, the immersion agent can not penetrate the closed porosity,

2. open porosity, accessible pores, describe by volume V_2, density of immersion agent ρ_2 and mass of immersion agent M_2,

3. solid particles, described by volume V_3, skeletal density ρ_3 and mass M_3.

In following part the final equation for porosity evaluation using known densities in three phase medium is derived. Let us first define ratio between volume of closed and open porosity as α, the porosity is defined as the pores volume to the total volume ratio.

$$\Phi = \frac{V_1 + V_2}{V}, \tag{2}$$

$$\alpha = \frac{V_1}{V_2}. \tag{3}$$

Second, mass is volume multiplied with density and the small pores are empty - the isooctane does not penetrate them. That means small pores do not have any mass,

$$V\rho = M, \tag{4}$$

$$V_1 + V_2 + V_3 = V, \tag{5}$$

$$M_2 + M_3 = M. \tag{6}$$

Substituting Eq. (4) to Eqs. (5), (6) leads to the Eqs. (7), (8)

$$V_2\rho_2 + V_3\rho_3 = V\rho, \tag{7}$$

$$V_2\rho_2 + (V - (V_1 + V_2))\rho_3 = V\rho. \tag{8}$$

Inserting Eq. (3) to Eq. (8) leads to

$$V_2\rho_2 + (V - (\alpha + 1)V_2)\rho_3 = V\rho, \tag{9}$$

$$V_2(\rho_2 - (\alpha + 1)\rho_3) = V\rho - V\rho_3. \tag{10}$$

From Eq. (10) the relation leads to the overall volume and density considering small and large pores respectively

$$V_2 = \frac{V(\rho - \rho_3)}{\rho_2 - (\alpha + 1)\rho_3}, \tag{11}$$

$$V_1 = \frac{\alpha V(\rho - \rho_3)}{\rho_2 - (\alpha + 1)\rho_3}, \tag{12}$$

$$V_1 + V_2 = \frac{V(\rho - \rho_3)}{\rho_2 - (\alpha + 1)\rho_3}(\alpha + 1). \tag{13}$$

Finally from Eq. (13), the formula for calculation of porosity from known skeletal density (ρ_3), bulk density (ρ), the density of medium in the large pores (ρ_2) and the ration between large and small pores, (α), arises out,

$$\Phi = \frac{V_1 + V_2}{V} = \frac{\rho - \rho_3}{\rho_2 - (\alpha + 1)\rho_3}(\alpha + 1). \tag{14}$$

In our case (in the geopolymer) it is considered that the porosity is distributed in the gel as well as in the fly ash. The smallest accessible pore radius for isooctane is 0.4 nm, assuming that the cross-sectional area of an isooctane molecule is 0.54 nm^2 [Radojević et al., 2002]. All larger pores are assumed to be accessible.

3.2 Porosity quantification

The evolution of porosity in alkaline activated fly ash during activation is not yet properly described in literature. The main goal of this work is experimentally measured development of the porosity during the polycondensation.

Literature introduces two different types of porosity, the terminology used in this work is adopted from the model describing ordinary Portland cement. At any stage of reaction, the hardened paste consists of N-A-S-H gel, unreacted precursor (fly ash, metakaolin) and the residue are water-filled spaces, [(Ed.) and van Deventer (Ed.), 2009].

1. These voids out of the gel are called capillary pores.

2. Within the gel itself, there exist interstitial voids, called gel pores.

The nominal diameter of gel pores is about 3 nm for C-S-H gel while capillary pores are one or two orders of magnitude larger. In our porosity assessment the pores are not divided to these two groups, but are measured only as quantitative total porosity.

A preliminary experiment of porosity quantification was focused on comparison of porosity measuring methods and source materials. As mentioned above five sets of specimens were created, each set consists from three specimens:

1. heat cured, ground FA

2. heat cured, non-ground FA

3. ambient cured, ground FA

4. ambient cured, non-ground FA

5. metakaolin.

The ambient cured specimens used in this experiment stayed six months hermetically closed in ampoules at the laboratory temperature (≈22°C). The heat cured specimens were exposed to 80°C prior to testing. Tab. 7 and Fig. 11 show the results of porosity measurements by different methods.

The porosity values introduced in Tab. 7 and in Fig. 11 were obtained by four methods, one MIP and three calculations from two measured densities.

1. MIP only

2. From He pycnometry obtained skeletal density ρ_{FA}^{sk}, from dried sample obtained ρ_{FA}^{b}, the porosity is calculated substituting into the Eq. (1).

3. From He pycnometry obtained skeletal density ρ_{FA}^{sk}, from by isooctane saturated sample obtained ρ_{FA}^{b}, the porosity is calculated substituting into the Eq. (1).

4. From dried sample obtained ρ_{FA}^{dry}, from by isooctane saturated sample obtained ρ_{FA}^{sat}, the porosity is calculated substituting into the Eq. (1), two equations with two unknowns occurs, additionally to the porosity can be also calculated the skeletal density.

Sample type /	Measured porosity			
Porosity assessment method	1.	2.	3.	4.
heat cured, ground FA	30.8 %	28.4 %	33.8 %	36.0 %
heat cured, non-ground FA	33.8 %	28.4 %	37.0 %	40.6 %
ambient cured, ground FA	29.6 %	23.6 %	30.8 %	33.6 %
ambient cured, non-ground FA	30.4 %	25.0 %	32.2 %	35.1 %
metakaolin	41.2 %	36.2 %	42.6 %	45.6 %

Table 7: Comparison of porosity obtained by different methods. [1] MIP. [2]-[4] calculated from two densities.

Another detailed experiment aimed at quantification of porosity during maturing of the samples. In this case only the ambient cured specimens made from non-ground fly ash were used. The heat cured specimens were unusable due to very fast reaction kinetics. The ground fly ash was not used due to demanding grinding process and possibility of introduction of error when grinding. Also the preliminary experiment shows, that there is not any

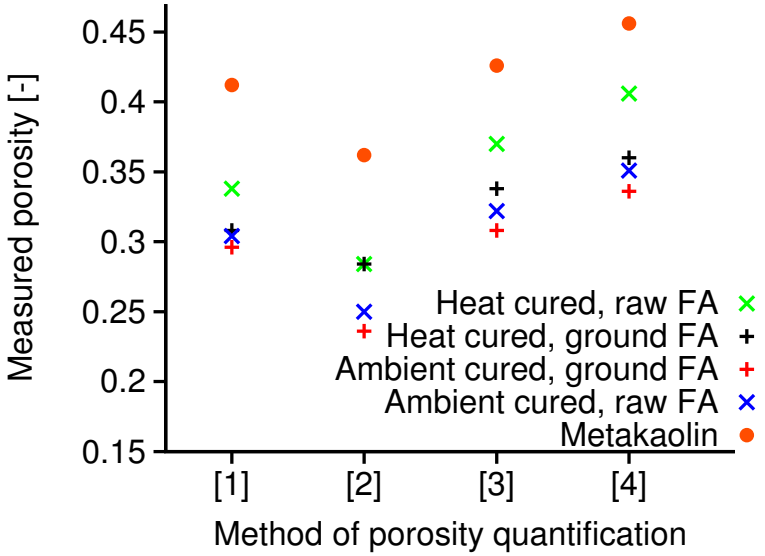

Figure 11: Comparison of porosity obtained by different methods. 1. MIP. 2.-4. calculated from two densities.

extreme difference between porosity when using raw or ground fly ash and the results correspond very well.

The ambient-curing proceeds at ambient temperature 22 °C. MIP and He pycnometry was performed two times, in 3rd and 12th week. The porosity development was measured in house after the given curing time in

- 2 weeks,
- 6 weeks,
- 12 weeks,
- 20 weeks.

The coherence of gel does not allow to measure earlier than two weeks after mixing. Two methods had been utilized, both used a known value of skeletal density obtained from He pycnometry and calculation of porosity substituting into Eq. (1). Immediately after mixing the porosity can be computed from known composition of the mixture.

First the samples were dried, measured and weighted. This gives the value of "total" porosity. Second the samples were submerged into isooctane and after saturation weighted. This gives by substituting into the three phase

medium, Eq. (14), the value of isooctane accessible porosity. The results of both methods are shown in Tab. 8 and Fig. 12, where DoR is reaction degree,

Sample age	DoR	TP	N-AP	η
1 week	0.327	33.34 %	7.32 %	0.220
6 weeks	0.397	34.77 %	4.33 %	0.125
12 weeks	0.420	32.00 %	0.47 %	0.015
20 weeks	0.442	32.07 %	0.00 %	0.000

Table 8: Accessible porosity

TP is total porosity, N-AP means isooctane not-accessible porosity and η is for the not-accessible to accessible porosity ratio $V_{N\text{-}AP}/V_{TP}$.

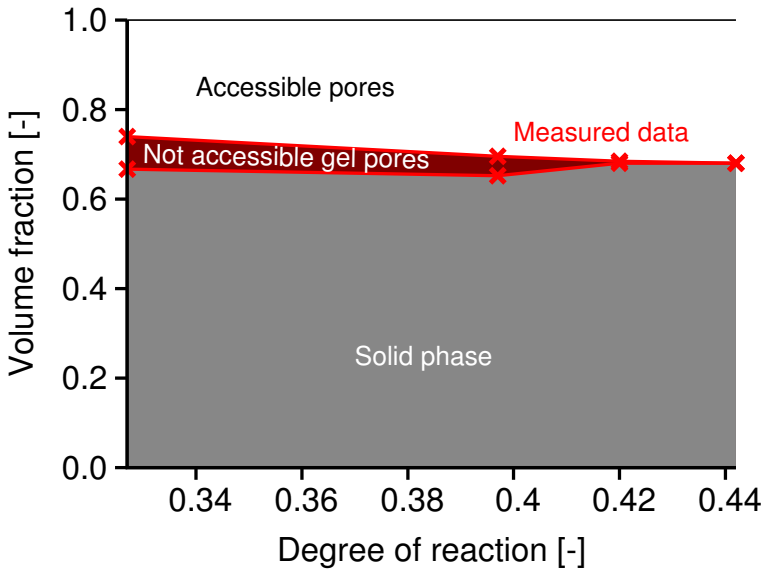

Figure 12: For isooctane accessible porosity development with respect to DoR

As mentioned above, the porosity was obtained from known composition of the mixture immediately after mixing. The fractions are fly ash, water glass and sodium hydroxide. The bulk density of the mixture was measured in 10 ml graduated cylinder, the density of activator solution (water glass and NaOH mixture) was obtained by pycnometer, the skeletal density of fly ash is known from the He pycnometry. The only one unknown is the porosity of fly ash immediately after mixture. Assuming that the activator is fully

evaporable (has no solid residuum), one obtains the initial porosity. The densities of compounds are introduced in Tab. 9. The density of Activation

Component	Density
Fly ash skeleton	2070 kg/m^3
Activator	1545 kg/m^3
Mixture	1752 kg/m^3

Table 9: Densities of compounds

solution was experimentally determined at Institute of Chemical Technology in Prague, department of Glass and Ceramics. The density of fly ash skeleton comes from He-pycnometry (Micromeritics AccuPyc 1330) measured at Institute of Chemical Process Fundamentals of the ASCR, Prague. The density of mixture was obtained from measured volume and mass immediately after mixing; the 15 ml graduated cylinder was fulfilled with the AAFA mixture and weighted. Initial volumes of the mixture fractions are given in table Tab. 10. The unknown value of fly ash density was computed. The porosity

Compound	Weight	Density	Volume
Mixture	730.32 g	1752 kg/m^3	0.417 l
Activator	230.32 g	1545 kg/m^3	0.149 l
Fly ash	500.00 g	**1867 kg/m^3**	0.268 l*

* $V_{FA}^{Initial}$

Table 10: Density of fly ash.

of fly ash can be now easily obtained by substituting the fly ash density and the fly ash skeletal density in the Eq. (14).

$$\begin{aligned} \Phi_{FA} &= \frac{\rho_{FA} - \rho_{FA}^{Skel}}{\rho_{Air} - \rho_{FA}^{Skel}} = \frac{1867 - 2070}{-2070} = 9.8\%, \\ V_{FA}^{Voids}(0) &= \Phi_{FA} \cdot V_{FA}^{Initial} = 0.098 \cdot 0.27\text{l} = 0.0265 \text{ l}. \end{aligned}$$

The volume of pores in FA added to the volume of activator results to the initial porosity,

$$\Phi = \frac{V_{FA}^{Voids} + V_{activator}}{V_{mixture}} = \frac{0.0265 + 0.149}{0.417} = 42.0\%. \qquad (15)$$

3.3 Reaction kinetics - Arrhenius equation

Let us introduce the degree of reaction as the rate between initial and consumed amount of fly ash. Direct simulation of DoR from a known chemical composition is beyond capabilities of presented models. Instead, the evolution of DoR is taken from experimental data of Fernández-Jimenéz [Fernández-Jiménez et al., 2004] who measured the DoR progress on AAFA samples activated with 8 M NaOH solution and cured at 85°C, see Fig. 13. The evolution of DoR was determined by an acid attack with HCl 1:20. Similar results were observed on calorimetric data, revealing that the ratio activator/fly ash is insignificant for the DoR and that a maximum reaction rate occurs at 8-10 minutes after the contact, substantially reduced after two hours at elevated temperatures [Palomo et al., 1999].

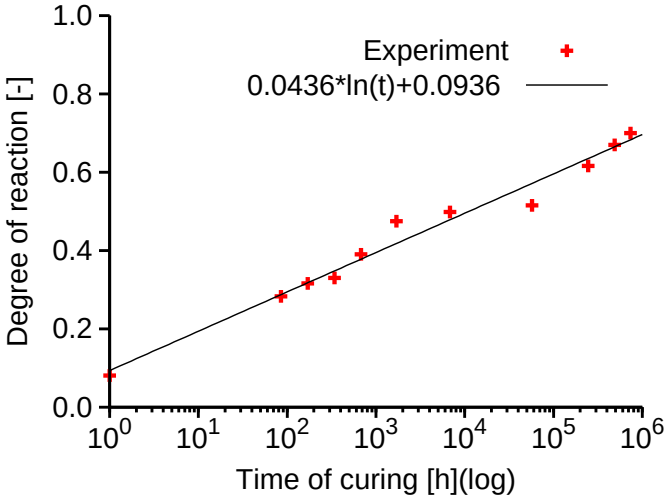

Figure 13: Determination of reaction degree as a function of time, 25°C, experiment by [Fernández-Jiménez et al., 2004].

The Arrhenius equation is used to recalculate a degree of reaction (DoR) for various curing temperatures. For example the temperature change from 85°C to 20°C causes slow down 400 times in reaction kinetics. The known relationship Eq. (16) was published for example in [Škvára et al., 2009] and takes the form,

$$\tau(T_{25}) = \tau(T_{85}) exp\left[\frac{E_a}{R}\left(\frac{1}{T_{25}} - \frac{1}{T_{85}}\right)\right] \tag{16}$$

where R is the universal gas constant $R = 8.314$ J/K mol and E_a is the activation energy. Skvara, [Škvára et al., 2009], measured for similar samples

the activation energy $E_a = 86.2$ kJ/mol. When the temperature of curing changes from 85°C to 25°C the Arrhenius equation predicts the scaling factor of 340.

3.4 Model of volumetric evolution

The model of volumetric evolution is based on measured porosities during activation of fly ash. The raw porosity data are introduced in the last chapter, this chapter proceeds further for the model formulation. Much inspiration about the volumetric evolution had been gathered from the Portland cement and the work of Powers and Brownyard [Powers and Brownyards, 1948]. Fig. 14 shows volumetric plots for Portland cement during curing period. Similar model was formulated for the AAFA, see Fig. 15. At the initial state,

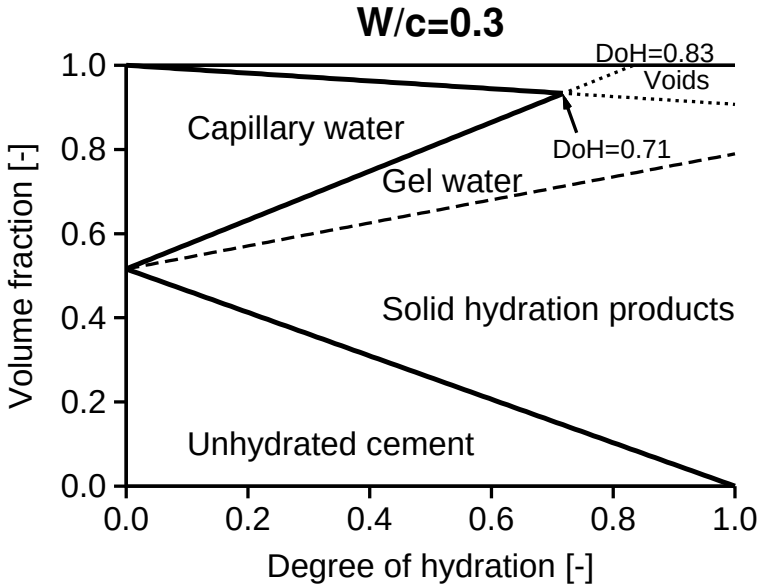

Figure 14: Volumetric model for OPC according to Powers [Powers and Brownyards, 1948].

at DoR = 0.0, no fly ash becomes activated, while a complete activation occurs at DoR = 1.0. To build a simple conceptual model describing basic phenomena, several assumptions of the volumetric model need, have to be made:

- The whole activator is treated in the form of evaporable water, disregarding a small solid part remaining after drying. Under saturation, open porosity is filled with evaporable water.

- No chemical shrinkage/expansion occurs so that the volumetric balance of all liquid and solid phases is maintained during the activation process.
- All reactions are time-independent and depend only on DoR. Such simplification neglects separate contribution of dissolution, precipitation and aging of N-A-S-H gel.

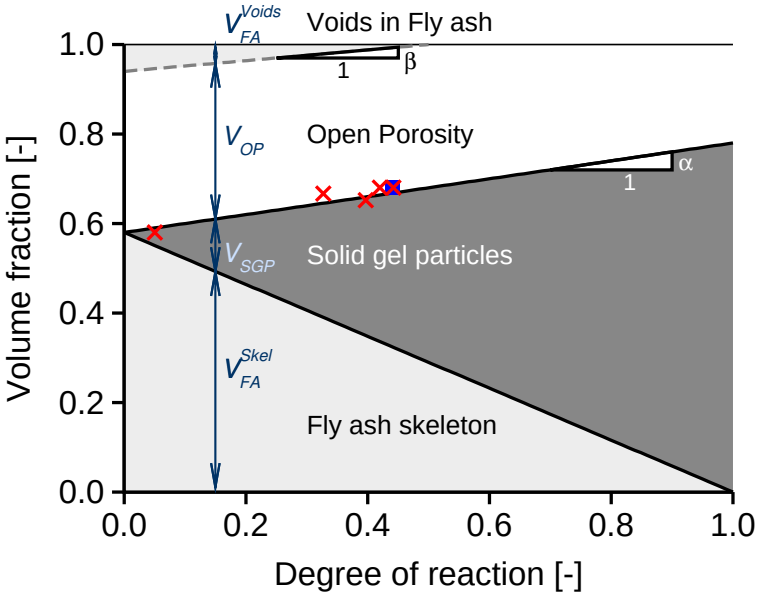

Figure 15: Volumetric model for AAFA.

The lines in Fig. 15 are described by equations:

$$V_{FA}^{Skel}(\mathrm{DoR}) = V_{FA}^{Skel}(0)\,[1-\mathrm{DoR}]\,, \tag{17}$$

$$V_{FA}^{Voids}(\mathrm{DoR}) = V_{FA}^{Voids}(0) - \beta\mathrm{DoR},\ V_{FA}^{Voids}(\mathrm{DoR}) \geq 0, \tag{18}$$

$$V_{SGP}(\mathrm{DoR}) = \left[V_{FA}^{Skel}(0) + \alpha\right]\mathrm{DoR}, \tag{19}$$

$$V_{OP}(\mathrm{DoR}) = 1 - V_{FA}^{Voids}(\mathrm{DoR}) - V_{FA}^{Skel}(0) - \alpha\mathrm{DoR}, \tag{20}$$

The Fig. 15 shows the possible volumetric evolution of different phases in the AAFA during activation. Following list introduces the three main phases in the model.

1. V_{FA}^{Skel} represents the volume fraction fly-ash skeleton. Voids persisting in the fly-ash after the mixing are quantified with V_{FA}^{Voids}. It must be noted that after a few minutes during the mixing, the activator

efficiently destroys a thin shell of plerospheres and opens their porosity, the so-called stage 1, see the introduction part in Section 1.4. This is manifested by partial loss of workability and heat release in isothermal calorimetry. Voids in the fly ash came from the combination of known skeletal density of fly ash, density of activating solution and measured volume, and weight of mixture immediately after the mixing process, see previous Section 3.2.

2. V_{SGP} is the volume fraction of solid gel particles. The term "gel" is intentionally unused due to the gel's composition from the solid and the liquid parts. No characteristic gel's porosity exist, hence the gel could be understand to contain both activator and solid gel particles.

3. V_{OP}, the volume of open porosity describes conveniently a part of accessible porosity by external water. The activator fills up the major part of open porosity.

Degree of reaction (DoR) presents a microstructural parameter, which describes the alkali-activation progress of fly ash. Expressing all reactions in terms of DoR is more convenient against time for two reasons:

- Circumventing a logarithmic time scale, needed for a proper plot .
- Mutual comparison for samples cured at various temperatures.

Parameters for Eqs. (17)-(20) had to be obtained experimentally. The volume of solid part of non reacted fly ash V_{FA}^{Skel} is given by the initial amount of FA in the mixture, see Eq. (15). The volume of voids in fly ash V_{FA}^{Voids} disappears roughly at DoR=0.5. The experimentally fitted parameters for the model Fig. 15 are introduced in Tab. 11.

Parameter	Value
V_{FA}^{Skel}	0.58
V_{FA}^{Voids}	0.06
α	0.2
β	0.12

Table 11: Experimentally determined parameters for the volumetric model.

3.5 Nanoindentation data

The micromechanical elastic properties of the phases were obtained from the nanoindentation realized at local faculty by Jiří Němeček, [Němeček et al., 2009]. Indentation was realized both at ambient and heat cured samples of AAFA and also on metakaolin samples for results comparison. For current study is most important the ambient cured AAFA sample. The results of heat cured samples and metakaolin indentation are mentioned only for comparison, the results shows that the reaction product does not depend on the curing method and on the source material respectively, see results Tab. 12.

Indentation moduli from 700 locations were gathered and recalculated to Young's moduli. The nanoindentation results are introduced on Fig. 16. The elastic moduli were statistically processed and the deconvolution results to four different Gaussian distributions. Deconvolution is globally an ill-posed problem and many possible solutions exist, however, the peak for N-A-S-H is clearly defined. Other phases are hypothesized to present partly activated slag and unreacted precursor.

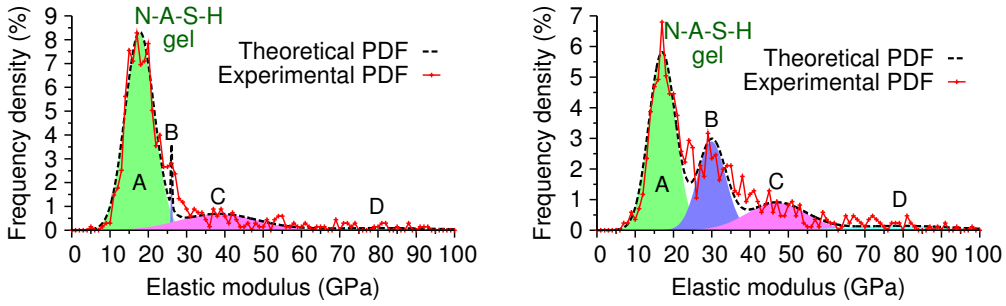

Figure 16: Elastic moduli determined by nanoindentation. Left ambient cured AAFA, right heat cured AAFA, data from [Němeček et al., 2009]. Peaks are hypothesized to represent A - N-A-S-H gel, B - Partly-activated slag, C - Nonactivated slag, D - Nonactivated compact glass.

3.6 Downscaling to solid gel particles

According to the volumetric model it is considered that the N-A-S-H gel is formed by the solid gel particles and evaporable water. Characterization of N-A-S-H gel was done by nanoindentation, see the previous Section. Tab. 13 shows the volume fractions, Young's moduli and a scatter of N-A-S-H gel determined by nanoindentation. The elastic properties of the solid gel particles can now be obtained by means of a downscaling process.

	AAFA		AAMK
	Heat-cured	Ambient-cured	Heat-cured
A.	17.03 ± 3.48 (50.7 %)	17.72 ± 3.75 (77.5 %)	17.72 ± 4.43 (97.2 %)
B.	29.95 ± 3.66 (26.6 %)	26.06 ± 0.18 (1.1 %)	
C.	46.90 ± 7.76 (17.6 %)	38.27 ± 10.13 (17.5 %)	
D.	79.15 ± 14.34 (5.1 %)	79.65 ± 16.99 (3.9 %)	
E.			43.91 ± 8.69 (2.8 %)

Table 12: Elastic moduli (GPa) of individual material phases in heat- and ambient-cured AAFA and heat-cured AAMK. The values in parentheses denote frequency. Taken from [Němeček et al., 2009]. A - N-A-S-H gel, B - Partly-activated slag, C - Nonactivated slag, D - Nonactivated compact glass, E - Unreacted metakaolin.

	AAFA		AAMK
	Ambient-cured	Heat-cured	Heat-cured
Young's modulus	17.72 ± 3.75 GPa	17.03 ± 3.48 GPa	17.72 ± 4.43 GPa
Volume fraction	77.50 %	50.70 %	97.20 %

Table 13: Elastic moduli of N-A-S-H gel originated from different precursors.

As mentioned above the N-A-S-H gel is formed by evaporable water and solid gel particles. The nanoindentation is considered to take place on DoR=0.44, at this DoR are known the volumetric fraction from the volumetric model. Evaporable water covers 0.485 and solid gel occupies 0.5185. The downscaling process was done with Mori-Tanaka homogenization. The Mori-Tanaka scheme for an isotropic spherical inclusion [Zaoui, 2002] runs with the reference phase of the gel particles. The elastic properties of the gel particles were fitted to reach the elastic properties of the N-A-S-H gel given by nanoindentation, see Tab. 13. Standard deviation of indentation moduli for the N-A-S-H gel, 17.72 ± 3.75 GPa, see Tab. 14, led to the variation of elastic properties of the solid gel particles, the resulting average Young's modulus is 49.8 GPa and Poisson's ratio 0.23, for the deviation see Tab. 14.

3.7 Two scale homogenization

The elastic properties of AAFA constituents given in Tab. 12 were connected with the volumetric model for alkali-activation. Two-level elastic homogenization seems to give reasonable results. At the first level, elastic

properties of the N-A-S-H gel, composed from the solid gel particles and evaporable water in the open porosity, were obtained using the Mori-Tanaka method with the reference phase of the solid gel particles. The second level homogenized the gel, fly ash and voids in the fly ash, by repeating the Mori-Tanaka method with the reference phase of the N-A-S-H gel.

The input data for homogenization are introduced in Tab. 14. The elastic properties of fly ash skeleton strongly depends on particle diameter, the value of 104 GPa is an average from range 82 GPa - 126 GPa given in [Matsunaga et al., 2002].

Parameter	Volume fraction [-]	Young's modulus [GPa]	Poisson's ratio [-]
$V_{FA}^{Skel}(0.44)$	0.324	104.0	0.20
$V_{FA}^{Voids}(0.44)$	0.001	0.001	0.001
$V_{OP}(0.44)$	0.325	0.001	0.499924
$V_{SGP}(0.44)$	0.350	38.2-49.8-59.5[a]	0.22-0.23-0.24[a]
Sum	1.000		

Table 14: Volumetric fractions at DoR = 0.44 and elastic properties of constituents. a) Three values stem from a standard deviation of N-A-S-H gel indentation moduli.

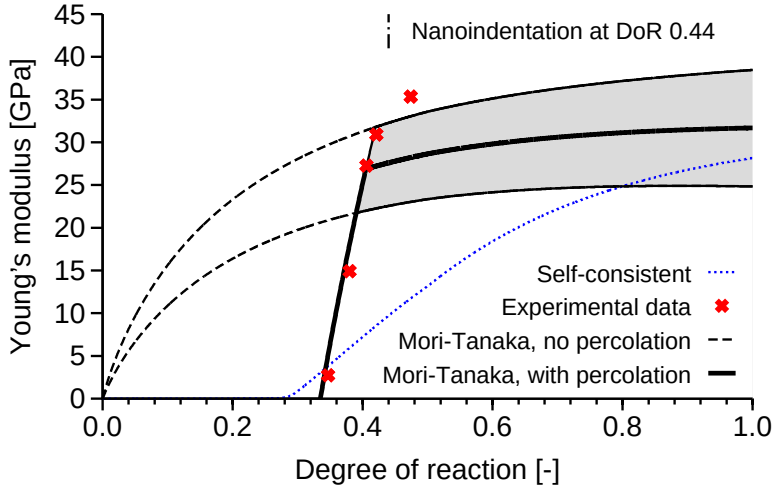

Figure 17: Homogenized Young's modulus for the AAFA.

Fig. 17 shows the results from two-scale homogenization at the final level. The experimental data originate from a non-destructive testing by a cyclic

loading. The load level reached approximately 0.3 of the ultimate load and the force acted uniaxially on prismatic samples 40 x 40 x 160 mm, equipped with a set of extensometers to control the bending.

Homogenization solely by Mori-Tanaka method shows really bad result in the initial phase of alkali-activation. The problems lies in percolation properties of true N-A-S-H gel. Until a minimal DoR is reached, which is called percolation threshold, the solid gel particles are mutually separated. The Mori-Tanaka model assumes perfect connection between the particles. This assumption is not fulfilled bellow the percolation threshold. The self consistent scheme is shown on the Fig. 17 only for comparison. In this method, the dominant phase is not specified as in the Mori-Tanaka method, but points back to the homogenized medium. The dominant phase at each time step is the with bigger volume. The beginning phase of the alkali-activation is perfectly described by this method. However, later elastic properties via the self-consistent scheme would be seriously underestimated, which denies its application. Percolation problems are known to occur in early ages of hydration in the system of Portland cement paste [Šmilauer and Bittnar, 2006]. Introduction of the percolation function in the form

$$p = (\mathrm{DoR}–\mathrm{DoR_p}), \tag{21}$$

allowed to capture the percolation threshold, $\mathrm{DoR_p}$, from which the N-A-S-H gel modulus becomes non-zero. The Young modulus from the first homogenization step (the modulus of N-A-S-H gel) is multiplied with Eq. (21). The percolation limits must be calibrated with experiment. Calibration yielded $\mathrm{DoR_p}$=0.335 and the upper limit at $\mathrm{DoR_p}$ = 0.405. Under the lower limit DoRp returns the percolation function zero. Above the upper limit plays percolation no role and Eq. (21) yields p=1. The thick line in Fig. 17 shows the elastic prediction in terms of average AAFA's modulus. When is considered the scatter in the properties of solid gel particles the range of validity arises and seems to cover almost all experimental points. In addition, the self-consistent scheme in Fig. 17 demonstrates that intrinsic percolation threshold associated with the scheme is in reasonable correlation with experimental data.

Fig. 18 shows elastic results from the first level homogenization, the level of N-A-S-H gel. Before $\mathrm{DoR_p}$=0.335, the percolation function returns a negligible elasticity. The percolation threshold occurs when the solid gel particles have the relative volume 0.4395, the volume fraction of the solid gel particles and open porosity is V_{SGP}=0.2613 and V_OP=0.3332 respectively. [Rintoul and Torquato, 1997] performed a numerical study in the system of identical (monodisperse) overlapping spheres, resulting in the percolation

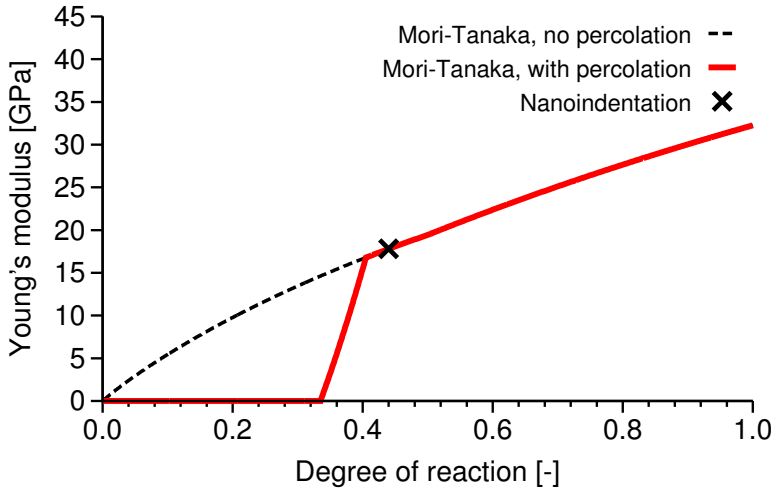

Figure 18: Homogenized Young's modulus for the N-A-S-H gel.

threshold 0.2895 $\pm$ 0.0005. The percolation threshold changes when a particle size distribution is taken into account. Two distinct sphere diameters were found to have the percolation threshold as high as 0.70 [Torquato, 2001]. It must be denoted that the N-A-S-H gel is continuously stiffening due to increasing fraction of solid gel particles. The presented model is based on a packing density of the solid gel particles and can not address changes within the particle, which may polymerize on the a stick scale.

4 AAFA usage in real structure

This section describes first large-size usage of alkali activation fly ash in the Czech Republic. All previous laboratory samples were prepared in well defined conditions using special equipment and all were in comparison with real structure size very small. Mixing, manipulation and curing in laboratory conditions could not sufficiently predict the behavior of the material in the real concreting plant and construction site.

The previous basic experiments carried out in the laboratory were only gel based, no filler was present. A size of specimens used was between micrometers (nanoindentation) to centimeters (samples for leaching measurement). Another group of experiments were the small sized samples of AAFA concrete, prisms sized about 10-50 cm. These specimens contains the AAFA binder and the aggregates as filler, similar to ordinary concrete. This group of experiments shows the ability of AAFA to replace the Portland cement in concrete. Thus a pilot experiment of about $3m^3$ was carried out. A ruined retaining wall Fig. 21 in a garden showed good ability to be replaced by AAFA concrete. For the AAFA concrete was used the same mixture as for the laboratory experiments, see Tab. 15. The mixture was optimized with respect to workability. The AAFA concrete was produced in CEMEX concreting plant in Beroun (20 km SW from Prague) Fig. 19, which is located approximately 5 km from the construction site.

The experiment shows excellent workability of the material directly after mixing, after about thirty minutes the material hardens very fast, Fig. 20. The ability to transport the AAFA concrete for longer time is not sufficient. Cubes designed for destructive test were prepared in the concrete plant. The retaining wall was constructed and will be long-time monitored. Up to date no efflorescence and no cracks have occurred except of acceptable shrinkage crack.

This large sized experiment was carried out in order to verify present knowledge in alkali activated materials. All experiments described in this section were done in cooperation with the Department of Construction Technology, CTU in Prague technologically coordinated by Ing. Rostislav Šulc.

Phase	Volume in 1 m^3	Volume in 0.33 m^3
Aggregates fraction 0/4 mm	750 kg	247.5 kg
Aggregates fraction 8/16 mm	500 kg	165 kg
Aggregates fraction 16/22 mm	470 kg	155 kg
Water	86.5 dm^3	28.5 dm^3
Fly ash	350 kg	115.5 kg
Water glass (16%)	120 dm^3	39.6 dm^3
Sodium hydroxide	28 kg	9.24 kg
Calcium hydroxide	11 kg	3.63 kg
Glenium AC 40	10.5 dm^3	3.5 dm^3
Air entrainment LP 75	1.05 dm^3	0.35 dm^3

Table 15: AAFA concrete mixture composition.

The following page presents a fotodocumentation from the retaining wall construction.

Figure 19: Left concreting plant, right flow test. Three cubic meters of AAFA concrete were produced, the volume of blender in the concreting plant is 0.33 m^3, eight mixtures had been done to fill the concrete agitator. The time elapsed between first and last mixture was approximately one hour.

Figure 20: The workability of AAFA concrete was not ideal one hour after mixing.

Figure 21: Wall before and after AAFA casting.

5 Simulation of AAFA leaching

Efflorescence presents a major problem in alkali-activated materials. After the activation, significant amounts of unreacted alkalies remain in the system, which can be leached via a slow diffusion process. The rate of leaching and the total amount of remaining alkalies have never been quantified before and present the main objective of this section. Numerical methods, particularly finite element approach, form the framework of this diffusivity simulation. The source data for the simulation came from the experiments carried out at the Institute of Chemical Technology in Prague at department of Glass and Ceramics.

5.1 Differential formulation of non-stationary diffusion equation

Let us consider a 1D element with axis x, volume Ω and boundary Γ. The non-stationary diffusion problem means that the concentration $w(x,t)$ inside the element changes with a respect to time. Assuming a homogeneous isotropic material with a diffusivity λ, the differential equation reads [Bažant, 1972],

$$\lambda \frac{\partial^2 w(\boldsymbol{x},t)}{\partial \boldsymbol{x}^2} = \frac{\partial w(\boldsymbol{x},t)}{\partial t}. \tag{22}$$

To solve Eq.(22), one needs to define boundary and initial conditions. The initial conditions define the concentration field at zero time, that means $w(\boldsymbol{x},0) = \overline{w}(\boldsymbol{x},0)$. The boundary conditions can appear in many forms, for example

- Dirichlet (or first-type) boundary condition, prescribing the concentration on the domain boundary

$$w(\boldsymbol{x},t) = \overline{w}(\boldsymbol{x},t) \text{ on the boundary } \Gamma, \tag{23}$$

- Neumann (or second-type) boundary condition specifies the ion flux across the boundary with outward normal n,

$$\frac{\partial w(\boldsymbol{x},t)}{\partial t} n = \overline{\frac{\partial w(\boldsymbol{x},t)}{\partial t}} \text{ on the boundary } \Gamma, \tag{24}$$

- supplementary boundary condition for the flux with respect to a ion transfer coefficient B at the surface given by Newton's law with a given concentration far from boundary layer $\overline{w}(\boldsymbol{x},t)$,

$$\frac{\partial w(\boldsymbol{x},t)}{\partial t} = B\left[w(\boldsymbol{x},t) - \overline{w}(\boldsymbol{x},t)\right] \text{ on the boundary } \Gamma. \tag{25}$$

5.2 FEM and time discretization

The solution of Eq.(22) proceeds using the FEM. A weak form stems from the principle of zero virtual work of the concentration over the element. The solution of Eq.(22) is fulfilled only in average at the volume Ω,

$$\int_{\Omega} \left[\frac{\partial w(x,t)}{\partial t} - \frac{\partial w^2(x,t)}{\partial x^2} \right] \delta w(x,t) dV = 0. \tag{26}$$

To fulfill the Dirichlet condition, Eq.(23) requires $\delta T(x,t)$ on the boundary Γ to be equal to zero. Applying the Green formula on Eq.(26) yields

$$\int_{\Omega} \frac{\partial w(x,t)}{\partial t} \delta w dV + \int_{\Gamma} \overline{\frac{\partial w(x,t)}{\partial t}} \delta w dV - \int_{\Omega} \frac{\partial w(x,t)}{\partial t} \delta \frac{\partial w(x,t)}{\partial x} dV = 0. \tag{27}$$

Let us divide the element to finite sections with volume Ω_e and approximate linearly the concentration and flux in each finite element

$$w(x) \approx \mathbf{N}\boldsymbol{w}, \tag{28}$$

$$\boldsymbol{q} = \frac{\partial w}{\partial x} \approx \mathbf{B}\boldsymbol{w} = \frac{\mathrm{d}\mathbf{N}}{\mathrm{d}x}\boldsymbol{w}, \tag{29}$$

where $\mathbf{N}$ is a linear interpolation function and the matrix $\mathbf{B}$ contains the derivatives of the interpolation functions. The virtual vector of concentrations is approximated in the same manner. Substituting Eqs. (28), (29) into the Eq.(27) yields the weak form,

$$\mathbf{C}\dot{\boldsymbol{w}} + \mathbf{K}\boldsymbol{w} = \boldsymbol{p}, \tag{30}$$

where the dot means time derivative and the vector $\boldsymbol{p}$ includes the boundary conditions. The used matrices are defined as

$$\mathbf{C} = \int_{\Omega} \mathbf{N}^T \mathbf{N} \mathrm{d}\Omega, \tag{31}$$

$$\mathbf{K} = \int_{\Omega} \mathbf{B}^T \lambda \mathbf{B} \mathrm{d}\Omega, \tag{32}$$

$$\boldsymbol{p} = -\int_{\Gamma} \mathbf{N}^T \overline{\boldsymbol{q}} \mathrm{d}\Gamma. \tag{33}$$

Time discretization approximates the nodal values $\boldsymbol{w}$ from Eq.(30) at all times using selected computed time points. The time evaluation points have a constant time difference, $t_i = i\Delta t$ for $i = 0, \ldots, T$. For the numerical integration, the parameter τ, which gives time point of derivative evaluation

during the time step. $\tau = 0$ means explicit method, the derivative from Eq.(30) is approximated by the slope in a last known time step t_i. $\tau = 1$ means unconditionally-stable implicit scheme, the derivative is obtained at time t_{i+1}. $\tau = 0.5$ means the Crank-Nicolson method and the derivative is evaluated in the middle of the time step.

The final equation for the 1D simulation takes the form,

$$\left(\frac{\mathbf{C}}{\Delta t} + \tau\mathbf{K}\right)\boldsymbol{w}_{i+1} - \tau\boldsymbol{p}_{(i+1)} = \left(\frac{\mathbf{C}}{\Delta t} + \tau\mathbf{K}\right)\boldsymbol{w}_i + (1-\tau)\boldsymbol{p}_i, \qquad (34)$$

where $\boldsymbol{w}_{(i+1)}$ are the unknown concentrations. All terms at the right hand side are known from the last time step.

5.3 Experimental data

All simulations aimed at description of leaching of Na^+ ions from alkali-activated fly ash specimens. Specimens sized $40 \times 40 \times 160$ mm were submerged into 600 ml of water for two weeks. The water was changed and the concentration of Na^+ ions was measured every 24 hours, except of weekends. Tab. 16 shows the measured concentrations of Na^+ ions in the water.

T	24	48	72	96	168	192	216	240	264	336	360	384	408	432
C	1090	733	557	422	812	307	236	214	197	365	168	143	132	119

Table 16: Na^+ ions leaching experimental results, T - Time [hours], C - Concentration [mg/l]. Measured by Lenka Myšková, Institute of Chemical Technology, Prague.

5.4 1D Simulation

The first simulation approximated the problem with 1D elements. The length of finite elements was 20 mm (the half of the shortest sample edge dimension) with the preservation of volume. The mathematical formulation derived above was implemented into Matlab/Octave code. Unknown value of diffusion coefficient was determined as the best fit to experimental data using the method of least squares. The value of ion transfer coefficient "B", see Eq. (25), was chosen to be 10 day^{-1}. The Fig. 22 shows, that the result of numerical simulation does not depend on the ion transfer coefficient when it's value is big enough, larger than approximately 1 day^{-1}. This has the physical meaning of prescribed concentration at the surface. In this case is

the ion flux not limited with the surface but only with the diffusivity. The Fig. 26 shows the distribution of concentration inside the body in the 1D case during leaching, the numbers means days of leaching. As mentioned above the diffusion coefficient was determined as the best fit to experimental data using the method of least squares with result of $5.7{\cdot}10^{-7}$ m^2/day.

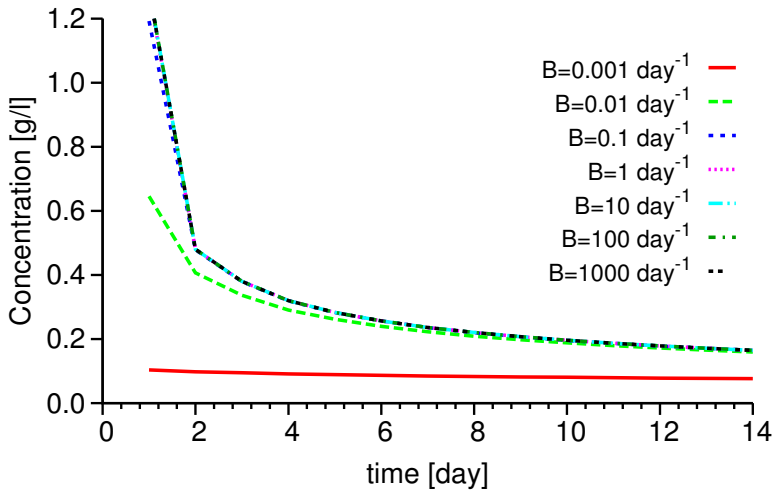

Figure 22: Leaching results from experiments and 1D and 3D simulation.

5.5 Verification with analytical solution

The nonstationary transport equation can be solved analytically in special simple case with following assumptions:

- infinite bath - zero concentration on surface,
- constant diffusion coefficient,
- infinite body,
- constant concentration at time zero.

The analytical solution stands out in the form of the error function see Eq. (35), [Vedalakshmi et al., 2009], where the $C^{Na^+}_{init}$ is the initial concentration of Na^+ in the body, the $C^{Na^+}(x,t)$ is the concentration in given time and at given position in the body and λ represents the diffusion coefficient. The comparison of 1D simulation and analytical solution is shown on Fig. 24. The 1D simulation shows excellent correspondence with analytical solution,

which is given by the formulation of problem and by the same idealization scheme.

$$\mathrm{C}^{\mathrm{Na}^+}(x,t) = \mathrm{C}^{\mathrm{Na}^+}_{init}\ \mathrm{erf}\left(\frac{x}{2\sqrt{\lambda t}}\right), \tag{35}$$

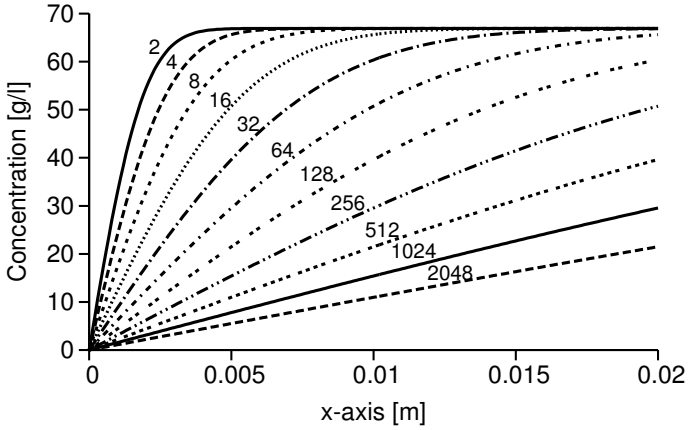

Figure 23: 1D analytical solution of Na^+ leaching.

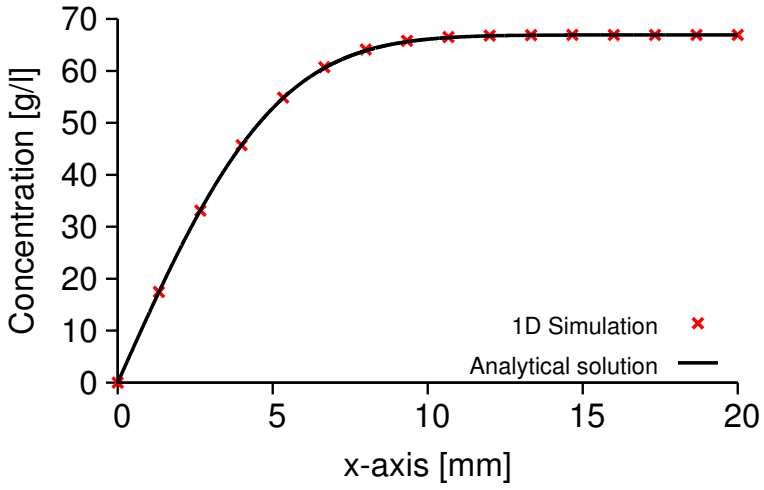

Figure 24: Verification of 1D simulation algorithm.

5.6 3D Simulation and results

More advanced 3D simulation was carried out in the OOFEM code made by B. Patzák, [Patzák and et al., 1993]. Geometry of specimen was meshed using linear brick elements. Only 1/8 of volume was considered due to symmetry of the problem; the reduced problem was represented with 20x20x80mm prism with three free boundaries (the middle of sample) and with three prescribed boundaries (the surface of experimental sample).

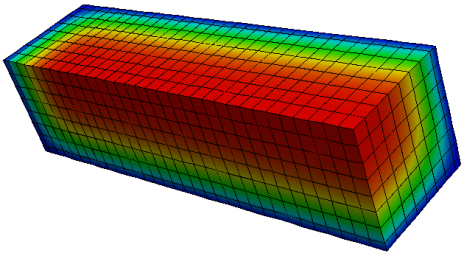

Figure 25: 3D simulation of Na^+ leaching.

The diffusion coefficient for Na^+ ions transport in the saturated state was identified to be 5.7 x10^{-5} m^2/day. Fig. 26 compares measured and computed concentrations.

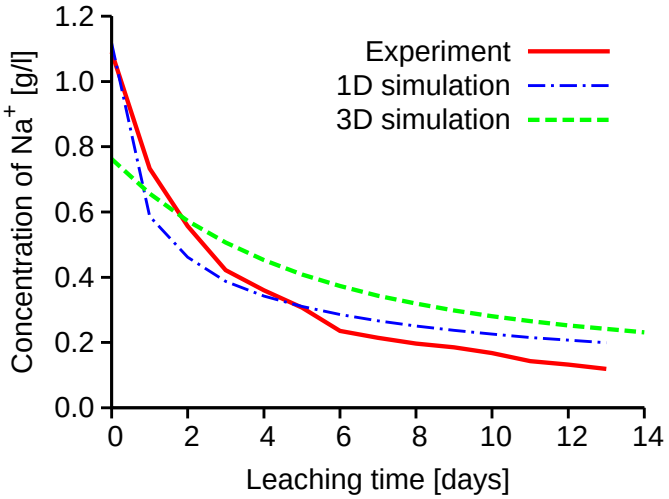

Figure 26: Leaching results from experiments and 1D and 3D simulation.

6 Conclusion

This work contributed to defined objectives in the following ways:

1. measured development of open porosity during maturing of AAFA.
2. formulated appropriate and simple model of AAFA volumetric evolution.
3. aligned intrinsic elastic properties to the phases of volumetric model.
4. formulated a multi-scale model which gives elastic properties on macro scale. Those properties were verified experimentally with excellent correspondence.
5. determined an unknown value of diffusion coefficient for Na^+ leaching.
6. assisted in construction of a retaining wall from AAFA concrete.

The results contribute to better understanding of the process of alkali activation. The combination of nanoindentation, micromechanical modeling and volumetric model applied to the alkali activated materials has never been described in literature. The models show, that a high DoR is a necessary to reach good mechanical performance of AAFA. At ambient curing temperature, this process takes roughly weeks, thus a heat curing seems to be a necessity to accelerate the reaction kinetics. This step complicates the usage of AAFA in large scale production.

The results of this work were presented on international conferences CIMTEC 2010 in Italy and Engineering Mechanics 2010 held in Svratka.

References

[Bažant, 1972] Bažant, Z. P. (1972). Thermodynamics of interacting continuua with surfaces and creep analysis of concrete structures. *Nuclear Engineering and Design*, 20:477–505.

[CEZ, 2010] CEZ (2010). CEZ home page. http://www.cez.cz.

[Constantinides et al., 2006] Constantinides, G., Chandran, K. S. R., Ulm, F.-J., and Vliet, K. J. V. (2006). Grid indentation analysis of composite microstructure and mechanics: Principles and validation. *Materials Science and Engineering*, A(430):189–202.

[CZSO, 2010] CZSO (2010). CZSO home page. http://www.czso.cz.

[Davidovits, 1999] Davidovits, J. (1999). Chemistry of geopolymeric systems, terminology. In *Geopolymer '99 International Conference*, pages 9–40, Saint Quentin, France.

[(Ed.) and van Deventer (Ed.), 2009] (Ed.), J. L. P. and van Deventer (Ed.), J. S. J. (2009). *Geopolymers: Structures, Processing, Properties and Industrial Applications*. Woodhead Publishing Ltd, first edition.

[Fernández-Jiménez et al., 2006a] Fernández-Jiménez, A., de la Torre, A. G., Palomo, A., López-Olmo, G., Alonso, M. M., and Aranda, M. A. G. (2006a). Quantitative determination of phases in the alkaline activation of fly ash. Part II: Degree of reaction. *The Science and Technology of Fuel and Energy*, 85(14-15):1960–1969.

[Fernandez-Jimenez and Palomo, 2003] Fernandez-Jimenez, A. and Palomo, A. (2003). Characterisation of fly ashes. Potential reactivity as alkaline cements. *Fuel*, 82:2259–2265.

[Fernández-Jiménez and Palomo, 2005] Fernández-Jiménez, A. and Palomo, A. (2005). Composition and microstructure of alkali activated fly ash binder: Effect of the activator. *Cem. Concr. Res.*, 35:1984–1992.

[Fernández-Jiménez et al., 2004] Fernández-Jiménez, A., Palomo, A., and Criado, M. (2004). Microstructure development of alkali-activated fly ash cement: a descriptive model. *Cem. Concr. Res.*, 35:1204–1209.

[Fernández-Jiménez et al., 2006b] Fernández-Jiménez, A., Palomo, A., Sobrados, I., and Sanz, J. (2006b). The role played by the reactive alumina content in the alkaline activation of fly ashes. *Microporous and Mesoporous Materials*, 91:111–119.

[Földvári, 1997] Földvári, M. (1997). Kaolinite-genetic and thermoanalytical parameters. *Journal of Thermal Analysis and Calorimetry*, 48(1):107–119.

[Gluchovskij, 1959] Gluchovskij, V. D. (1959). *Gruntosilikaty*. Gosstrojizdat USSR, Kiev.

[Glukhovsky, 1959] Glukhovsky, V. D. (1959). *Soil Silicates (Gruntosilikaty)*. Kiev, Budivelnik publisher, USSR.

[Hardjito and Rangan, 2005] Hardjito, D. and Rangan, B. V. (2005). Development and properties of low-calcium fly ash-based geopolymer concrete. Research report gc 1, Curtin University of Technology, Perth, Australia. Faculty of Engineering.

[Kynčlová, 2006] Kynčlová, M. (2006). *Geopolymerní betony, možnosti využití v konstrukcích pozemních staveb*. Diplomová práce, CVUT, Praha.

[Matsunaga et al., 2002] Matsunaga, T., Kim, J. K., Hardcastle, S., and Rohatgi, P. K. (2002). Crystallinity and selected properties of fly ash particles. *Materials Science and Engineering A*, 325(1-2):333 – 343.

[Němeček, 2009] Němeček, J. (2009). Creep effects in nanoindentation of hydrated phases of cement pastes. *Materials Characterization*, 60(9):1028 – 1034.

[Němeček et al., 2009] Němeček, J., Šmilauer, V., and Kopecký, L. (2009). Elastic properties of alkaline activated fly ash: results from nanoindentation and micromechanical modeling.

[Palomo et al., 1999] Palomo, A., Grutzeck, M. W., and Blanco, M. T. (1999). Alkali-activated fly ashes. A cement for the future. *Cem. Concr. Res.*, 29:1323–1329.

[Patzák and et al., 1993] Patzák, B. and et al. (since 1993). Object Oriented Finite Element Method - OOFEM. http://www.oofem.org.

[Pecheco-Torgal et al., 2008] Pecheco-Torgal, F., ao Castro-Gomes, J., and Jalali, S. (2008). Alkali activated binders: A rewiew part 1. historical background, terminology, reaction mechanism and hydration products. *Construction and science materials*, 22(1):1305–1314.

[Perera et al., 2007] Perera, D., Uchida, O., Vance, E., and Finnie, K. (2007). Influence of curing schedule on the integrity of geopolymers. *Journal of Materials Science*, 42(9):3099–3106.

[Powers and Brownyards, 1948] Powers, T. C. and Brownyards, T. L. (1948). Studies of physical properties of hardened portland cement paste. Bulletin 22, Research Laboratories of the Portland Cement Association, Chicago.

[Radojević et al., 2002] Radojević, M., Jović, V., , and Vitorović, D. (2002). Study of sepiolite from goleš (kosovo, yugoslavia). i. sorption capacity. *J.Serb.Chem.Soc.*, 67(7):489–497.

[Rintoul and Torquato, 1997] Rintoul, M. and Torquato, S. (1997). Precise determination of the critical threshold and exponents in a three-dimensional continuum percolation model. *J. Phys. A: Math. Gen.*, 30:585–592.

[Sakamoto et al., 2003] Sakamoto, T., Shibata, K., Takanashi, K., Owari, M., and Niheic, Y. (2003). Analysis of surface composition and internal structure of fly ash particles using an ion and electron multibeam micro-analyzer. *Applied Surface Science*, pages 762–766.

[Škvára et al., 2009] Škvára, F., Kopecký, L., Šmilauer, V., and Bittnar, Z. (2009). Material and structural characterization of alkali activated low-calcium brown coal fly ash. *Journal of Hazardous Materials*, 168:711–720.

[Šmilauer and Bittnar, 2006] Šmilauer, V. and Bittnar, Z. (2006). Microstructure-based micromechanical prediction of elastic properties in hydrating cement paste. *Cem. Concr. Res.*, 36(9):1708–1718.

[Survey, 2009] Survey, U. G. (2009). Historical statistics for mineral and material commodities in the united states: U.s. geological survey data series 140, available online at http://pubs.usgs.gov/ds/2005/140/.

[Torquato, 2001] Torquato, S. (2001). *Random Heterogeneous Materials. Microstructure and Macroscopic Properties.* Springer-Verlag New York.

[Vedalakshmi et al., 2009] Vedalakshmi, R., Saraswathy, V., Song, H.-W., and Palaniswamy, N. (2009). Determination of diffusion coefficient of chloride in concrete using warburg diffusion coefficient. *Corrosion Science*, 51(6):1299 – 1307.

[Škvára et al., 2009] Škvára, F., Kopecký, L., Šmilauer, V., and Bittnar, Z. (2009). Material and structural characterization of alkali activated low-calcium brown coal fly ash. *J. of Hazardous Materials*, 168:711–720.

[Škvára et al., 2008] Škvára, F., Svoboda, P., Doležal, J., Bittnar, Z., Šmilauer, Kopecký, L., and Šulc, R. (2008). Geopolymer concrete - an ancient material too? *Ceramics - Silikáty*, 52(4):296–298.

[Šmilauer et al., 2010] Šmilauer, V., Němeček, J., , Kopecký, L., Škvára, F., and Hlaváček, P. (2010). Application of micromechanics on alkali-activated materials.

[Wallah and Rangan, 2006] Wallah, S. E. and Rangan, B. V. (2006). Low-calcium fly ash-based geopolymer concrete: Long term properties. Research Report GC 2, Curtin University of Technology, Perth, Australia.

[Xu and van Deventer, 2000] Xu, H. and van Deventer, J. S. J. (2000). The Geopolymerisation of Alumino-Silicate Minerals. *International Journal of Mineral Processing*, 59(3):247–266.

[Zaoui, 2002] Zaoui, A. (2002). Continuum Micromechanics: Survey. *Journal of Engineering Mechanics*, 128(8):808 – 816.

[Zhang et al., 2009] Zhang, Y., Li, Z., Sun, W., and Li, W. (2009). Setting and Hardening of Geopolymeric Cement Pastes Incorporated with Fly Ash. *ACI Materials Journal*, 106(5):405 – 412.